SURFACE ALIGNMENT OF AN ELASTIC BODY USING A MULTI-RESOLUTION WAVELET REPRESENTATION

Smadar Gefen, Student Member, IEEE, Oleh Tretiak*, Senior Member, IEEE,

Louise Bertrand, Glenn D. Rosen, Jonathan Nissanov

Abstract **- An algorithm for nonlinear registration of an elastic body is developed. Surfaces (outlines) of known anatomic structures are used to align all other (internal) points. The deformation field is represented with a multi-resolution wavelet expansion and is modeled by the partial differential equations of linear elasticity. A hierarchical approach that reduces algorithm complexity is adopted. The performance of the algorithm is evaluated by alignment of sections of mouse brains located in the olfactory bulbs. The wavelet alignment algorithm produced a 2.0 to 5 - fold improvement in accuracy over an affine (linear) alignment algorithm.**

Index Terms **– Elastic deformation, nonlinear registration, wavelet, segmentation.**

This work was supported by NIH Award P20 MH62009.

S. Gefen and O. Tretiak are with the Electrical and Computer Engineering Department, Drexel University, 3141 Chestnut St. Philadelphia, PA 19104 (tel: 215-8952214,email: tretiak@ece.drexel.edu).

L.Bertrand and J.Nissanov are with the Computer Vision Laboratory for Vertebrate Brain Mapping, Department of Neurobiology and Anatomy, Drexel College of Medicine, Drexel University, 2900 Queen Lane Philadelphia, PA 19129-1096.

Glenn D. Rosen is with the Department of Neurology, Beth Israel Deaconess Medical Center, Harvard University, 330 Brookline Ave., Boston, MA 02215.

I. INTRODUCTION

Image registration is a widely required task in multi-dimensional data visualization and analysis. In medicine image alignment is used to fuse complementary information (across subjects and modalities as well as within), and to construct a probabilistic map. Image registration as a general solution in computer vision and in biomedicine in particular has been widely explored [1-3]. Four main characteristics distinguish one registration algorithm from another: (1) the features that drive the registrations – these can be image-based or geometric; (2) the transformation model, whether it is a linear or nonlinear; (3) the similarity measures based on which the alignment accuracy is determined; and (4) the optimization method with which the transformation parameters are estimated. Survey papers dealing with the classification of registration methods can be found in the literature (see [4-7]).

A common biomedical problem where image registration has been employed is in mapping newly acquired experimental datasets (called the *test brains*) onto a canonical atlas (called the *reference brain*). By doing so, one can segment these sets using standard neuro-anatomical templates. Registration of biomedical images, for this purpose and in general whenever inter-subject alignment is contemplated, is complicated by the inevitable presence of geometric variability. This necessitates use of nonlinear transformation if significant accuracy is desired. In addition, corresponding features used to guide registration are difficult to identify.

A number of approaches have been adopted to compensate for nonlinear differences between objects to be aligned including modeling one object as an elastic deformed version of the other. Among these are many that relied on Duchon [8] and Meinguet [9] introduction of the thin-plate splines as a mathematical interpolator. Goshtasby [10] and Bookstein [11] applied this interpolator to 2D image registration. Gabrani and Tretiak [12, 13] extended Bookstein's method to 3D image registration. In the thin-plate splines method the image is modeled as a metal plate in which landmark points are deformed in the x and y directions separately. Coefficients of radial basis functions that interpolate the deformation are computed such that an elastic energy functional is minimized.

In contrast to the mathematical thin-plate method, the Navier linear partial differential equation (PDE) is a physical model of nonlinear elastic deformation. The Navier PDE modeling of organ tissues as an elastic object, adopted from continuum mechanics, considers the organs as an elastic mediums that are exposed to external forces and are smoothly deformed. Bajcsy and Broit [14, 15] were the first to apply Navier PDE to registration. In their method an equilibrium state between external and internal forces was reached for an isotropic homogeneous body. The external forces were determined in such a way that an image-based similarity metric is maximized. Similarly, Davatzikos [16] used a deformable surface parametric representation of the brain's external surface to map one brain surface onto another based on extracted surface (geometric) features. The elastic mapping of one brain volume to another was found by solving the differential equation that models an inhomogeneous elastic body under external forces. The external forces were determined so that the known cortical mapping was satisfied.

In the nonlinear registration case, where many registration parameters are involved, mis-registration might occur due to the difficulty in finding a global minimum in the presence of many local minima. The coarse-to-fine strategy in the optimization process can prevent convergence into local minima traps. Lester [7] classified nonlinear hierarchical registration methods based on a gradual increase in data complexity, warp complexity, and model complexity. An alternative representation of the elastic deformation signal is wavelet multi-resolution representation. The wavelet, being an inherently hierarchical representation of a signal, is naturally suitable for such progressive (coarse-to-fine) optimization starting from the low-resolution approximation of the signal (global deformation), through the details in its different orientations, and ending with the finest details of the signal (local deformation).

In this study we have used wavelets to represent the deformation which was modeled as a combination of components that range between global deformations (best represented by the lower resolution levels of the wavelet decomposition) and local deformations (best represented by the higher resolution levels of the wavelet decomposition). The wavelet coefficients that correspond to each different signal component were estimated separately and progressively, starting from global deformation down to local deformation. This progressive approach for recovering the deformation signal is effective for

reducing algorithm complexity. The elastic deformation of each signal component was estimated by minimizing the elastic energy (which is equivalent to solving for the static homogenous Navier PDE) as well as by minimizing the sum of squared distances between corresponding surfaces (which is equivalent to imposing boundary conditions).

The wavelet-based registration method presented here is characterized as follows: (1) the algorithm is driven by geometrical features with the brain's external and internal surfaces used to guide the registration algorithm; (2) the transformation model is a nonlinear deformation field where the region within the brain's volume is modeled by a wavelet multi-resolution representation; (3) the similarity metric used is based on the squared sum of distances where a distance is the interval between a point on the test surface and the closest point to it on the reference surface; and (4) the Marquardt-Levenberg (M-L) optimization algorithm is used to minimize a functional that is the sum of two terms, namely the sum of squared distances and the elastic energy. While the alignment algorithm formulated here is a two-dimensional version, its generalization into a three-dimension one is straightforward. The performance of the algorithm was demonstrated for the 2D case of mouse brain mapping, focusing on the olfactory bulbs, a brain area where sensory information from the nose is processed.

Wavelets have been used by several researchers for the application of image registration, either in order to represent the non-linear deformation between two images [17, 18] or to represent the intensities of images' pixels [19]. Amit [17] used wavelet basis as well as Fourier basis to represent the deformation. Amit used a gradient descent optimization method to minimize the mean of squared distances between intensities of corresponding pixels. Similarly, Downie [18] used a simulated annealing optimization method to find the wavelet coefficients that minimize the sum of squared distances between intensities of corresponding pixels. Both algorithms, [17] and [18], are image-based and as such most suited for applications dealing with intra-modality scans. In contrast, the registration algorithm, developed in this study, is based on geometric features; alignment is guided by objects' contours and surfaces and therefore can be used for applications dealing with inter- as well as intra- modality scans.

The rest of the paper is organized as follows. Section II presents applicable aspects of wavelet multi-resolution analysis. Next, in Section III, the registration algorithm is described. Algorithm evaluation with synthetic data is presented in Section IV. Section V evaluates the application of registration for the anatomical localization of internal structures within the olfactory bulbs of mouse brains. Section VI concludes with a discussion and suggestions for future research.

II. WAVELET REPRESENTATION OF THE ELASTIC DEFORMATION

In a registration algorithm the objective is to find the registration parameters that result in the best geometric correspondence between the *test object* and the *reference object*. Let us define an elastic deformation field **u**(**x**), represented by wavelet decomposition. In a registration procedure, we look for the wavelet parameters' vector, **c**, that yields:

$$\begin{aligned} x' &= x + u^1(x, y; \mathbf{c}) \\ y' &= y + u^2(x, y; \mathbf{c}) \end{aligned},$$

where (x, y) are coordinates in the test object space and (x', y') are corresponding coordinates in the reference object space. The registration algorithm find **c** by minimizing the sum of Euclidian distances between the test object's points and the reference object's points as well as the elastic energy of the deformation. Details are provided in Section III.

As mentioned above, the elastic deformation is represented by a wavelet multi-resolution approximation. The theory of Multi-Resolution Analysis (MRA) can be found in many sources (see [20], [21], [22], and [23] for example). The two-dimensional separable wavelet decomposition of a deformation signal, **u**(**x**), everywhere within a rectangular support **N**=(N_x,N_y) is presented in (1).

$$\begin{aligned} u(\mathbf{x})^i &= \sum_{\mathbf{k}=0}^{\mathbf{N}_J-1} 2^{-J} c_{J\mathbf{k}}^{i1} \Phi^1(2^{-J}\mathbf{x}-\mathbf{k}) + \sum_{j=R}^{J} 2^{-j} \sum_{s=2}^{4} \sum_{\mathbf{k}=0}^{\mathbf{N}_j-1} c_{j\mathbf{k}}^{is} \Phi^s(2^{-j}\mathbf{x}-\mathbf{k}), \\ \mathbf{N}_j &\equiv 2^{-j}\mathbf{N} = 2^{-j}(N_x, N_y), \quad \mathbf{k} = (k_x, k_y), \quad \mathbf{x} = (x, y), \quad i = 1,2 \end{aligned} \tag{1}$$

The basis functions are two-dimensional functions that are translated across a rectangular grid, with intervals of 2^j and within a support of **N**= (N_x,N_y). Each basis function is weighted by the corresponding

wavelet coefficient $c_{j\mathbf{k}}^{is}$. The basis functions are a tensor product of the one-dimensional *scaling* and *wavelet* functions as in (2) and as shown in Fig. 1 for the orthogonal *Coiflets* wavelet [23].

$$\begin{aligned}\Phi^1 &= f(2^{-j}x-k_x)f(2^{-j}y-k_y)\\ \Phi^2 &= f(2^{-j}x-k_x)y(2^{-j}y-k_y)\\ \Phi^3 &= y(2^{-j}x-k_x)f(2^{-j}y-k_y)\\ \Phi^4 &= y(2^{-j}x-k_x)y(2^{-j}y-k_y)\end{aligned} \tag{2}$$

The superscript index, "*s*", in (1) marks the sub-band (quadrant/orientation) in the wavelet decomposition space.

MRA theory states that a signal that approximated by its projection into space V_{R-1} can be equivalently represented by its projection into a lower resolution level space V_J and the difference spaces $W_R+W_{R+1}+\ldots+W_J$. The range of resolution levels, *J* to *R*, in the signal multi-resolution representation is determined by the application and by the signal's nature.

In general, the number of parameters $c_{j\mathbf{k}}^{is}$ is the same as the number of grid points in the represented signal rectangular support. For example, for a support of $\mathbf{N}=(N_x,N_y)=(128,128)$, 128x128=16384 parameters are required to represent the deformation in one direction. This is a large number of parameters to handle for most minimization algorithms. But, since the signal of interest - the elastic deformation - is by its nature smooth, lower resolution levels can be chosen to represent it with reasonable accuracy. For example, the signal's wavelet decomposition when using four resolution levels, *J*=6 to *R*=3, contains 32x32=1024 parameters. In order to further reduce the number of parameters the optimization algorithm deals with at a time, we split the wavelet coefficients into groups classified by the sub-band and the level of resolution they represent. Each such group of wavelet coefficients corresponds to a different component of the deformation. In other words, the deformation is a combination of components with different levels of details (resolution levels) and orientations (sub-bands). A progressive approach is applied in which the wavelet coefficients that correspond to a low resolution signal

component were estimated first and the wavelet coefficients that correspond to a high resolution signal component were estimated last. Fig. 2 shows the order in which the wavelet coefficients were optimized.

III. ALGORITHM DESCRIPTION

The registration of one elastic object to its homologue is done by estimating the nonlinear deformation that brings together a pair of corresponding surfaces. The deformation is determined by the registration parameters - the wavelet coefficients $c_{j\mathbf{k}}^{is}$ - that minimize the functional $E(\mathbf{c})$. We define a functional $E(\mathbf{c})$ which is a weighted sum of the sum of squared distances, $e(\mathbf{c})$, and the elastic energy, $L(\mathbf{c})$: $E(\mathbf{c}) = e(\mathbf{c}) + w \cdot L(\mathbf{c})$. The parameter w is a weight constant that is empirically determined. The functional $E(\mathbf{c})$ is a function of the registration parameters $c_{j\mathbf{k}}^{is}$ where s=1,…,4 and j=R,…,J. The full expression to $E(\mathbf{c})$ includes terms that depend on products of pairs of $c_{j\mathbf{k}}^{is}$ coefficients with different s and j values. We found that these terms are small [24], therefore we express $E(\mathbf{c})$ as $E(\mathbf{c}) = \sum_{s,j} [e(\mathbf{c}_j^s) + w \cdot L(\mathbf{c}_j^s)]$, where $\mathbf{c}_j^s \equiv [\mathbf{c}_j^{1s^T}, \mathbf{c}_j^{2s^T}]^T$ and $\mathbf{c}_j^{is}$ is a vector containing the wavelet coefficients within the j level of resolution and the s orientation and for the deformation in the direction i. Sections A and B below present the derivations of $e(\mathbf{c}_j^s)$ and $L(\mathbf{c}_j^s)$ as a function of the registration parameters. In the subsections below, for simplicity, we will refer to $\mathbf{c}_j^s$, $e(\mathbf{c}_j^s)$, and $L(\mathbf{c}_j^s)$ as $\mathbf{c}$, $e(\mathbf{c})$ and $L(\mathbf{c})$, respectively.

A. e(c) – Sum of Squared Distances

The distance between two points, $d_m \equiv d(T(\mathbf{x}_m, \mathbf{c}), S_r)$, is the Euclidean distance between an already mapped point on the test surface $\mathbf{a}(\mathbf{c}) \equiv T(\mathbf{x}_m, \mathbf{c})$ and the closest point to it, $\mathbf{x}'_m$, on the reference surface S_r. Similarly, a vector distance is defined as $\mathbf{v}_m \equiv \mathbf{a}(\mathbf{c}) - \mathbf{x}'_m$. Note that $d_m = \|\mathbf{v}_m\|$. The magnitude being minimized is the sum of the squared distances:

$$e(\mathbf{c}) = \sum_{m=1}^{M} d_m^2 = \sum_{m=1}^{M} d(T(\mathbf{x}_m, \mathbf{c}), S_r)^2 \tag{3}$$

Local dependency of $e(\mathbf{c})$ on the registration parameters, $\mathbf{c}$, is achieved by substituting the Taylor expansion of d_m in the vicinity of $\mathbf{c}_l$ *as* follows:

$$\begin{aligned} e(\mathbf{c}) &\approx \sum_{m=1}^{M} [d_m^2(\mathbf{c}_l) + 2 d_m(\mathbf{c}_l) \Delta^T \operatorname{grad}_c d_m(\mathbf{c}_l) + \Delta^T \operatorname{grad}_c d_m(\mathbf{c}_l) \operatorname{grad}_c d_m(\mathbf{c}_l)^T \Delta] \\ &= e(\mathbf{c}_l) + \Delta^T \mathbf{b} + \frac{1}{2} \Delta^T \mathbf{A} \Delta \end{aligned}, \tag{4}$$

where:

$$\mathbf{b}_i \equiv 2 \sum_{m=1}^{M} d_m(\mathbf{c}_l) \frac{\partial d_m(\mathbf{c}_l)}{\partial c_i}, \quad A_{ij} \equiv 2 \sum_{m=1}^{M} \frac{\partial d_m(\mathbf{c}_l)}{\partial c_i} \frac{\partial d_m(\mathbf{c}_l)}{\partial c_j}, \quad \text{and} \quad \Delta \equiv (\mathbf{c} - \mathbf{c}_l).$$

Following the chain rule of differentiation $\frac{\partial d_m(\mathbf{c}_l)}{\partial c} = \operatorname{grad}_{\mathbf{a}} d_m \cdot \frac{\partial \mathbf{a}}{\partial c}$. It was shown in [25] that $\operatorname{grad}_{\mathbf{a}} d_m = \frac{\mathbf{v}_m}{d_m}$. It follows that:

$$\frac{\partial d_m(\mathbf{c}_l)}{\partial c} = \frac{\partial d_m(\mathbf{c}_l)}{\partial c_{\mathbf{jk}}^{is}} = \frac{v_m{}^i}{d_m} \Phi^s(2^{-j} \mathbf{x}_m - \mathbf{k}).$$

B. $L(\mathbf{c})$ *– Elastic Energy*

The second term, $L(\mathbf{c})$, that is being minimized is the elastic energy:

$$L(\mathbf{c}) = \int [m \sum_{j=1}^{2} \sum_{i=1}^{2} \left(\frac{\partial u^i}{\partial x_j} \right)^2 + (m + l) \left(\frac{\partial u^1}{\partial x_1} + \frac{\partial u^2}{\partial x_2} \right)^2] d\mathbf{x} \tag{5}$$

where m and l are the Lame's coefficients that reflect the elastic properties of the medium. Expanding with $m = 1$ and $l = 0$ yields:

$$L(\mathbf{c}) = \int [2 \left(\frac{\partial u^1}{\partial x_1} \right)^2 + \left(\frac{\partial u^1}{\partial x_2} \right)^2 + \left(\frac{\partial u^2}{\partial x_1} \right)^2 + 2 \left(\frac{\partial u^2}{\partial x_2} \right)^2 + 2 \frac{\partial u^1}{\partial x_1} \frac{\partial u^2}{\partial x_2}] d\mathbf{x} \tag{6}$$

Substituting the signal as represented in (1) results in a linear combination of the integral:

$$h_{pq}^{st}(j,l,\mathbf{k},\mathbf{n}) = \int \frac{\partial \Phi^s(2^{-j}\mathbf{x}-\mathbf{k})}{\partial x_p} \; \frac{\partial \Phi^t(2^{-l}\mathbf{x}-\mathbf{n})}{\partial x_q} d\mathbf{x},$$

where p,q=1,2. (An analytic evaluation of this integral is presented in [24].) In order to simplify the expression for the elastic energy we assume that the scaling and wavelet functions used satisfy a principle we call *threefold orthogonality* [24]. The threefold orthogonality property states that the scaling and wavelet functions are orthogonal to each other and orthogonal to each other's first and second derivatives. The consequence of satisfying this property of triple orthogonality is that minimizing the elastic energy of the deformation is equivalent to minimizing separately the elastic energy of the different deformation components.

Let us continue and develop the expression in (6) for the signal component $u^i(j,s) = \sum_{\mathbf{k}=0}^{\mathbf{N}_j-\mathbf{1}} c_{j\mathbf{k}}^{is} \Phi^s(2^{-j}\mathbf{x}-\mathbf{k})$. In this case, (6) is a linear combination of the following terms:

$$\int [\frac{\partial u^i}{\partial x_p}\frac{\partial u^l}{\partial x_q}] d\mathbf{x} = \sum_{\mathbf{n}}\sum_{\mathbf{k}} c_{jk}^{is} c_{jn}^{ls} \int \frac{\partial \Phi^s(2^{-j}\mathbf{x}-\mathbf{k})}{\partial x_p}\frac{\partial \Phi^s(2^{-j}\mathbf{x}-\mathbf{n})}{\partial x_q} d\mathbf{x} =$$
$$\sum_{\mathbf{n}}\sum_{\mathbf{k}} c_{jk}^{is} c_{jn}^{ls} h_{pq}^{s}(j,\mathbf{k},\mathbf{n}) \equiv \mathbf{c}_j^{is\,T} \mathbf{Q}_{jpq}^{s} \mathbf{c}_j^{ls} \qquad (7)$$

Accordingly, the energy of the signal portion that corresponds to level j and orientation s is:

$$L(\mathbf{c}) = \mathbf{c}_j^{1s\,T}(2\mathbf{Q}_{j11}^{s} + \mathbf{Q}_{j22}^{s})\mathbf{c}_j^{ls} + \mathbf{c}_j^{2s\,T}(\mathbf{Q}_{j11}^{s} + 2\mathbf{Q}_{j22}^{s})\mathbf{c}_j^{2s} + 2\mathbf{c}_j^{1s\,T}\mathbf{Q}_{j12}^{s}\mathbf{c}_j^{2s} \qquad (8)$$

The matrix form of (8) is:

$$L(\mathbf{c}) = \begin{bmatrix} \mathbf{c}_j^{1s\,T} & \mathbf{c}_j^{2s\,T} \end{bmatrix} \cdot \begin{bmatrix} 2\mathbf{Q}_{j11}^{s} + \mathbf{Q}_{j22}^{s} & \mathbf{Q}_{j12}^{s} \\ \mathbf{Q}_{j12}^{s} & \mathbf{Q}_{j11}^{s} + 2\mathbf{Q}_{j22}^{s} \end{bmatrix} \cdot \begin{bmatrix} \mathbf{c}_j^{1s} \\ \mathbf{c}_j^{2s} \end{bmatrix} = \mathbf{c}^T \mathbf{Q}_j^{s} \mathbf{c} \qquad (9)$$

We proceed with applying the Taylor expansion of $L(\boldsymbol{c})$ in the vicinity of $\boldsymbol{c}_l$ to (9):

$$\begin{aligned} L(\mathbf{c}) &\cong \mathbf{c}_l^{\,T}\mathbf{Q}_j^{s}\mathbf{c}_l + (\mathbf{c}-\mathbf{c}_l)^T 2\mathbf{Q}_j^{s}\mathbf{c}_l + (\mathbf{c}-\mathbf{c}_l)^T\mathbf{Q}_j^{s}(\mathbf{c}-\mathbf{c}_l) \\ &= \mathbf{c}_l^{\,T}\mathbf{Q}_j^{s}\mathbf{c}_l + \Delta^T 2\mathbf{Q}_j^{s}\mathbf{c}_l + \Delta^T\mathbf{Q}_j^{s}\Delta \end{aligned} \qquad (10)$$

It can be shown that the matrix $\mathbf{Q}_j^s$ is linearly proportional to the Wavelet-Galerkin discretization matrix of the homogenous static Navier PDE [24]. This implies that minimizing the elastic energy is equivalent to solving the Navier PDE. The dimension of the matrix $\mathbf{Q}_j^s$ is $[2(2^{-j}N_x \cdot 2^{-j}N_y), 2(2^{-j}N_x \cdot 2^{-j}N_y)]$. Hence, in the higher levels of resolution, the matrix $\mathbf{Q}_j^s$ is large and sparse. Note though that the matrix $\mathbf{Q}_j^s$ depends only on the chosen support, **N**, and the scaling and wavelet basis functions Φ_j^s. $\mathbf{Q}_j^s$ does not depend on the object of interest (more specifically the object's deformation). Therefore it can be computed once offline and then used for the deformation estimation of any input object data. Sparsity of the matrix $\mathbf{Q}_j^s$, as a result of the locality of the wavelet basis functions, contributes to the reduction of algorithm complexity both in terms of storage and computation time. For example, the density of the $\mathbf{Q}_3^s$ matrix (percent of non-zero matrix elements out of all matrix elements) is 35%.

C. Parameters Optimization

The expressions developed above for the sum of the squared distances, $e(\mathbf{c})$, and for the elastic energy, $L(\mathbf{c})$, are combined to result in the functional $E(\mathbf{c})$:

$$E(\mathbf{c}) = e(\mathbf{c}) + w \cdot L(\mathbf{c}) \approx e(\mathbf{c}_l) + \mathbf{c}_l{}^T \mathbf{Q}\mathbf{c}_l + \Delta^T(\mathbf{b} + 2w\mathbf{Q}\mathbf{c}_l) + \frac{1}{2}\Delta^T(\mathbf{A} + 2w\mathbf{Q})\Delta . \qquad (11)$$

The overall minimization algorithm had as input two sets of contour points: the test set and the reference set. These were aligned with an affine transform [26]. A range of wavelet resolution can be used for the alignment — typically; we used levels 6 to 3. The estimated wavelet coefficients included only those that correspond to wavelet basis functions whose support overlapped the test contour points. Starting with zero for coefficient values, an iterative procedure was used to compute coefficients that minimized the energy functional defined in (11). Iteration was both within and across resolution levels, using the M-L algorithm [27]. For example, returning to the typical case using levels 6 to 3, about 20 M-L iterations

were performed within each level and stepping through levels of resolution in the following order: 6, 5, 6, 5, 4, 6, 5, 4, 3. Each iteration included computing the locations of the deformed test points, finding the closest points to these on the reference contour, and evaluation of matrix **A** and vector **b**, as in equation (11).

Using a coarse-to-fine approach, first we solve for the coefficients $\hat{\mathbf{c}}_J^1$ considering only the lowest resolution level, where $j=J$ and $s=1$. Next, we proceed to the second sub-band, $s=2$ (still at the same resolution level, $j=J$), solving for $\hat{\mathbf{c}}_J^2$. In the same manner we solve for the other two sub-bands, $s=2$ and $s=4$, at resolution level $j=J$. We proceed down the pyramid to the next level of resolution $j=J-1$, solving for the different sub-bands at this level, $s=2,3,4$. Hence, the computation of the wavelet coefficients is done progressively until the estimation of all coefficients is completed (see Fig. 2).

This coarse-to-fine approach, enabled due to the wavelet local and multi-resolution representation, offers important computational advantages: scalability and adaptability. Two factors contribute to the approximation error: the smoothness of the deformation and the wavelet resolution level. The approximation error is proportional to $c \cdot (2^j)^p \left\| \mathbf{u}^{(p)}(\mathbf{x}) \right\|$, where the constant c and the exponent p depend on the choice of wavelet [21]. Thus, the smaller j is, the smaller the approximation error. Consequently, there is a trade-off between accuracy of the deformation approximation and the algorithm complexity. The more resolution levels the algorithm uses to estimate the elastic deformation, the more accuracy will be achieved and the more storage and computation time will be required. This algorithm scalability is discussed further in Section IV.

The degree of smoothness of the deformation signal, $\left\| \mathbf{u}^{(p)}(\mathbf{x}) \right\|$, also contributes to the estimation error. Due to the locality of the wavelet representation, irregular regions in the deformation signal will affect the error only locally. Hence, there might be a situation where the error is small everywhere except for these local regions. In this case, using a higher resolution level only at these regions will reduce the

overall error without introducing large increase in complexity. This algorithm allows the use of an adaptive grid, although this option was not implemented in the current algorithm.

IV. ALGORITHM EVALUATION

The evaluation of the registration algorithm developed in this study was done by applying a known transformation to two closed contours - an ellipse and the external contour of a rat brain section – referred to as the test objects. These test objects were centered at a 128x128 rectangular support for which the deformation $\boldsymbol{u}(\mathbf{x})$ was defined. Three transformations were applied to the test objects to create the reference objects: (1) displacement $T_d(\mathbf{x})$, (2) affine transformation $T_a(\mathbf{x})$, and (3) affine and elastic transformation $T_a(\mathbf{x})+T_e(\mathbf{x})$. The three transformations were defined as follows:

$$\begin{aligned} T_d(\mathbf{x}) &= \mathbf{x} + [5,5]^T; \\ T_a(\mathbf{x}) &= \begin{bmatrix} 1.05 & -0.05 \\ 0.02 & 0.95 \end{bmatrix}\mathbf{x} + [5,5]^T; \\ T_e(\mathbf{x}) &= \begin{bmatrix} \cosh(a)(\cos b + \sin b) + \cosh(b)(\cos a + \sin a) - 2 \\ \sinh(a)(\cos b - \sin b) - \sinh(b)(\cos a - \sin a) \end{bmatrix} + \mathbf{x}, \end{aligned} \tag{12}$$

where $a = 0.2(x - \bar{x})$ and $b = 0.2(y - \bar{y})$. The elastic transformation, which is an analytic solution of the homogenous static Navier PDE, was scaled to result in an average and a maximum deformation along the objects' external contour that is about 5% and 15% of object radius, respectively.

The above transformations were applied to points along the test contour $\mathbf{x}_{test}$ to result in the reference contour $\mathbf{x}_{ref} = T(\mathbf{x}_{test})$. The objective was to estimate the applied deformation everywhere within the test object. Contour Error (CE) was defined as the distance between a point at the test contour and the closest point to it at the corresponding reference contour, whereas Actual Error (AE) is the distance between a test point and the corresponding reference point. We evaluated both errors because in the experimental setting we do not know the actual point correspondence and therefore the AE is unknown. Note that, by definition, the CE is always smaller than the AE.

In Fig. 3 the test objects: (a) ellipse and (b) rat brain section, the mapped test objects (that resulted in by applying the estimated deformation to the test object), and the reference objects (that resulted in by applying the analytic deformation to the test object) are shown. Fig. 3 shows the distance between mapped test objects to the reference objects for concentric layers within each reference object. The average Initial Deformation (ID), CE, and AE are shown in Table I. We see that the algorithm can recover almost completely translational transformation; the alignment error for $T_d(\mathbf{x})$ is much smaller than the errors for other transformations, and the alignment error for the rat brain is smaller than that for the ellipse. We believe that for a complex object's surface (in this case a rat brain section) more information is provided about actual correspondence than for a symmetric object's surface (in this case ellipse). In the case of rat brain section, the algorithm yields for an average ID of 7.1 pixels an average AE of 0.35 pixels and an average CE of 0.27 pixels.

One of the wavelet-based alignment algorithm advantageous characteristic is scalability. There is a trade-off between accuracy of deformation approximation and algorithm complexity. This trade-off can be controlled by the number of resolution levels one chooses to include in the deformation estimation. Table II shows the maximum number of registration parameters (wavelet coefficients) that reside at each orientation and at each resolution level of the wavelet decomposition. Since only coefficients that correspond to basis functions that overlap an object's boundary were estimated the actual number of registration parameters that were estimated is lower than the maximum.

Figures 4 and 5 show the relative AE (ratio of AE and ID) and the relative CE (ratio of CE and ID) where affine and elastic transformations were applied to the rat section, respectively. The relative errors are shown for different resolution levels and as a function of section's concentric layers (external layer (1) through internals layers (2-20)). Table III shows the relative error on the external contour and the algorithm's complexity as a function of the resolution levels number. The trade-off between approximation accuracy and algorithm complexity is apparent; the more deformation estimation accuracy is desired the more registration parameters and algorithm running time are required. The running times

reported in Table III are based on algorithm implementation using Matlab (version 6.1) on a Pentium IV computer (1.7 GHz, 1G Byte RAM).

V. EXPERIMENTAL RESULTS

A. Data Acquisition

Eleven mouse brains (genetic strain C57BL/6J) were studied. One, the *reference* brain, was used to construct a three dimensional brain volume atlas [28]. The other ten brains are the *test* brains. The test brains were embedded in celloidin and serially sectioned coronally as described in [29]. Briefly, brains were dehydrated through a graded series of ethanol and ethanol/ether baths before being embedded in celloidin. The brains were cut coronally into 30 μm sections and every section saved. Floating sections were stained with cresyl violet, and every section was mounted on glass slides, and cover slipped with Permount.

The performance of the registration algorithm was evaluated in the two-dimensional setting. A matching reference section for each test section was defined visually using the MacOStat software package [30]. Three pairs of such corresponding 2D coronal sections were defined from three different locations - rostral, intermediate and caudal levels of the olfactory bulbs as is shown in Fig. 6. The high morphological variability between corresponding sections is clearly evident. Nineteen anatomical structures (see Table IV for structures' Nomenclatures based on the Franklin and Paxinos atlas [31].) were manually delineated on these sections, as shown in Fig. 6. The delineation of the test section was done on images at a resolution of 4.3μm/pixel while that of the reference brain at a resolution of 8.7 μm/pixel.

B. 2D Registration of Sections from the Olfactory Bulbs of the Mouse Brains

As mentioned above, three coronal sections were selected from each of ten experimental brains. Each section was aligned to its matching reference section. To do so a subset of the manually delineated contours were used to guide the alignment process and the remaining ones were used for performance evaluation. Two performance measures were computed for each structure and averaged across the ten

brains: *error* (average residual distance between corresponding contours) and *overlap* (area of overlap of corresponding structures divided by the area of the reference structure). The error and overlap were computed for the data before the nonlinear alignment (after an affine transform was applied) and after the wavelet alignment.

Two cases for wavelet alignment were examined, Case I and Case II. In Case I the external contour alone guided the registration while in Case II the alignment was guided by the external contour as well as some internal ones. Tables IV, V, and VI contain the results (the structures that guide the registration are denoted in bold). The three rows at the bottom of tables IV, V, and VI show averages over all structures, weighted by structure area. We tabulate averages for registration guiding (RG) structures, for registration validating (RV) structures, and for all structures (Total).

As can be seen from Tables IV, V, and VI the reduction of the error is substantial: on average (for all sections combined) from 3.4 to 1.5 for Case I and to 0.6 for Case II. The average increase in the overlap between corresponding structures is from 75% to 83% for Case I and to 91% for Case II. Fig. 7 shows sample images of alignment. The images in Fig. 7 show the reference sections and their structures' contours in dashed/blue lines. On the top of each section are drawn the contours of the corresponding mapped test section where structures used to drive the alignment are shown in red and structures used for validation are shown in green. In the presence of high shape variability the improvement of Case II over Case I is apparent.

V. CONCLUSION

A registration algorithm that compensates for nonlinear differences between two homologues elastic objects is presented. The application of wavelet multi-resolution representation to the elastic deformation enabled complexity reduction of the optimization algorithm. The locality of the basis functions produced sparse matrices and the wavelet multi-resolution allowed separate handling of the optimization procedure for parameters of different signal components. The method developed in this study, validated with synthetic data, shows satisfactory results. The effectiveness of this registration

algorithm as a means for anatomical localization of internal structures in the olfactory bulbs of mouse brains was examined. This algorithm for brain mapping results in a promising performance in spite of having to overcome two main problems. The first is the large anatomical variability between corresponding structures in two different brains as is evident from Fig. 6. The second problem was that the registration algorithm was applied to two-dimensional sections. Registration of two homologous sections (instead of registration of two brain volumes) requires the intermediate step of extracting two corresponding sections from the brain volumes. Since the elastic deformation that a test brain undergoes is in three dimensions, it is not plausible to have a test section that corresponds fully to an in-plane reference section. Therefore, modeling elastic deformation is likely to be more accurate when applied in the three-dimensional case. The generalization of the algorithm presented in this study into three-dimensions is straightforward. In the future we plan to make this extension and evaluate the performance.

FIGURE CAPTIONS

Fig. 1. The four separable 2D wavelet basis functions based on orthogonal *Coiflets* wavelet.

Fig. 2. The progressive order in which registration parameters were estimated.

Fig. 3. The test object: (a) Ellipse and (b) rat brain section (in blue), overlapped by the mapped test object (in red), and the reference object (in dotted green).

Fig. 4. (a) Relative actual error, AE/ID, and (b) relative contour error, CE/ID, where an affine transformation was applied to the rat section. The errors are shown for different resolution levels and as a function of concentric layers (external layer (1) through internals layers (2-20)).

Fig. 5. (a) Relative actual error, AE/ID, and (b) relative contour error, CE/ID, where an elastic transformation was applied to the rat section. The errors are shown for different resolution levels and as a function of concentric layers (external layer (1) through internals layers (2-20)).

Fig. 6. Matching coronal sections from the atlas (left) and an experimental brain (right). The top pair located at a rostral level, the second pair located at an intermediate level, and the bottom pair located at a caudal level of the olfactory bulbs.

Fig. 7. Reference sections and their structures' contours are shown in dashed/blue lines. On the top of each section are drawn the contours of the corresponding mapped test section where structures used to drive the alignment are shown in red and structures used for validation are shown in green.. Case I (left) and Case II (right) are shown for caudal section (top), intermediate section (middle), and rostral section (bottom).

TABLE CAPTIONS

TABLE I: AVERAGE INITIAL DEFORMATION (ID), CONTOUR ERROR (CE), AND ACTUAL ERROR (AE) WHEN APPLYING TRANSLATION (T_D), AFFINE (T_A), AND ELASTIC (T_E+T_A) TRANSFORMATIONS TO AN ELLIPSE AND TO A RAT BRAIN SECTION (ERRORS ARE MEASURED IN PIXELS)

TABLE II: NUMBER OF REGISTRATION PARAMETERS AT EACH RESOLUTION LEVEL AND AT EACH ORIENTATION OF THE WAVELET DECOMPOSITION

TABLE III: RELATIVE ERROR ON EXTERNAL CONTOUR AND ALGORITHM COMPLEXITY FOR THE REGISTRATION OF RAT SECTIONS INCLUDING DIFFERENT RESOLUTION LEVELS

TABLE IV: LIST OF THE EXTERNAL/INTERNAL STRUCTURES IN THE MOUSE OLFACTORY

TABLE V: THE AVERAGE ERROR AND OVERLAP RATIO OF ROSTRAL SECTIONS FOR AFFINE AND WAVELET ALIGNMENT

TABLE VI: THE AVERAGE ERROR AND OVERLAP RATIO OF INTERMEDIATE SECTIONS FOR AFFINE AND WAVELET ALIGNMENT

TABLE VII: THE AVERAGE ERROR AND OVERLAP RATIO OF CAUDAL SECTIONS FOR AFFINE AND WAVELET ALIGNMENT

TABLE I
AVERAGE INITIAL DEFORMATION (ID), CONTOUR ERROR (CE), AND ACTUAL ERROR (AE) WHEN APPLYING TRANSLATION (T_D), AFFINE (T_A), AND ELASTIC (T_E+ T_A) TRANSFORMATIONS TO AN ELLIPSE AND TO A RAT BRAIN SECTION (ERRORS ARE MEASURED IN PIXELS)

	Ellipse			Rat Brain Section		
trans.	ID	CE	AE	ID	CE	AE
T_d	7.071	0.246 E-7	0.246E-7	7.071	0.178 E-7	0.178 E-7
T_a	7.708	0.323	0.481	7.074	0.106	0.143
T_e+ T_a	7.101	0.351	0.586	7.074	0.271	0.351

TABLE II
NUMBER OF REGISTRATION PARAMETERS AT EACH RESOLUTION LEVEL AND AT EACH ORIENTATION OF THE WAVELET DECOMPOSITION

Resolution level	Max Param. No.	Estimated Param. No.
6	4	4
5	16	16
4	64	64
3	256	230
2	1024	495
1	4096	1015

TABLE III
RELATIVE ERROR ON EXTERNAL CONTOUR AND ALGORITHM COMPLEXITY FOR THE REGISTRATION OF RAT SECTIONS INCLUDING DIFFERENT RESOLUTION LEVELS

Resolution Levels	CE	AE	Params. No.	Time (secs)
6	0.062	0.146	32	71
6 to 5	0.044	0.107	128	157
6 to 4	0.020	0.082	512	279
6 to 3	0.012	0.075	1084	466

TABLE IV
LIST OF THE EXTERNAL/INTERNAL STRUCTURES IN THE MOUSE OLFACTORY

The Olfactory Bulbs Anatomical Structures	
Structure	**Description**
GrO	granule layer, olfactory bulb
E/OV	ependyma & olfactory ventricle
aci	anterior commissure, intrabulbar
IPl	internal plexiform layer, olfactory bulb
Mi	mitral cell layer, olfactory bulb
EPl	external plexiform layer, olfactory bulb
Gl	glomerular layer, olfactory bulb
AOE	anterior olfactory nucleus, external
vn	vomeronasal nerve
EPlA	external plexiform layer accessory olfactory bulb
MiA	mitral cell layer, olfactory bulb
AOL	anterior olfactory nucleus, lateral
AOM	anterior olfactory nucleus, medial
AOD	anterior olfactory nucleus, dorsal
dlo	dorsolateral olfactory tract
GlA	glomerular layer, accessory olfactory bulb
lo	lateral olfactory tract
AOV	anterior olfactory nucleus, ventral
OB	olfactory bulb

TABLE V
THE AVERAGE ERROR AND OVERLAP RATIO OF ROSTRAL SECTIONS FOR AFFINE AND WAVELET ALIGNMENT

	Affine (linear)		**Case I (wavelet)**		**Case II (wavelet)**	
Structure	**Error**	**Overlap**	**Error**	**Overlap**	**Error**	**Overlap**
GrO	3.25	0.87	3.16	0.86	**0.14**	**1.00**
IPl	3.24	0.21	3.11	0.22	0.55	0.73
Mi	3.18	0.25	2.98	0.26	0.75	0.70
EPl	3.06	0.70	2.37	0.80	1.37	0.92
Gl	3.16	0.66	0.77	0.83	1.04	0.72
OB	**3.19**	**0.91**	**0.33**	**0.99**	**0.16**	**1.00**
RG*	3.19	0.91	0.33	0.99	0.16	1.00
RV+	3.13	0.60	2.35	0.71	0.86	0.85
Total	3.16	0.75	1.36	0.84	0.52	0.92

* registration guiding structures, + validation guiding structures

TABLE VI
THE AVERAGE ERROR AND OVERLAP RATIO OF INTERMEDIATE SECTIONS FOR AFFINE AND WAVELET ALIGNMENT

	Affine (linear)		Case I (wavelet)		Case II (wavelet)	
Structure	**Error**	**Overlap**	**Error**	**Overlap**	**Error**	**Overlap**
GrO	3.52	0.83	3.52	0.83	**0.18**	**1.00**
E/OV	2.84	0.26	3.18	0.26	1.67	0.50
aci	2.98	0.31	3.07	0.31	1.17	0.58
IPl	3.63	0.26	3.57	0.26	0.60	0.77
Mi	3.61	0.23	3.53	0.23	0.91	0.61
EPl	3.57	0.75	3.21	0.75	1.69	0.91
Gl	3.48	0.71	1.68	0.71	1.27	0.74
OB	**3.38**	**0.99**	**0.33**	**0.99**	**0.15**	**1.00**
RG	3.40	0.92	0.33	0.99	0.15	1.00
RV	3.47	0.60	2.95	0.67	1.02	0.85
Total	3.43	0.76	1.67	0.83	0.59	0.92

TABLE VII
THE AVERAGE ERROR AND OVERLAP RATIO OF CAUDAL SECTIONS FOR AFFINE AND WAVELET ALIGNMENT

	Affine (linear)		Case I (wavelet)		Case II (wavelet)	
Structure	**Error**	**Overlap**	**Error**	**Overlap**	**Error**	**Overlap**
GrO	2.74	0.80	2.72	0.82	**0.26**	**0.97**
E/OV	2.12	0.40	2.15	0.43	1.71	0.50
aci	2.24	0.47	2.23	0.49	1.14	0.61
IPl	1.87	0.26	1.73	0.28	0.65	0.65
Mi	2.05	0.28	1.92	0.32	0.97	0.63
EPl	2.69	0.70	2.40	0.75	1.96	0.83
Gl	2.38	0.49	2.12	0.58	2.24	0.56
AOE	4.46	0.40	4.77	0.34	2.59	0.75
vn	3.83	0.42	3.42	0.45	3.68	0.51
EPlA	3.60	0.30	3.76	0.25	2.64	0.35
MiA	4.84	0.33	4.91	0.30	3.30	0.52
AOL	3.46	0.75	3.65	0.76	**0.20**	**0.97**
AOM	3.74	0.44	3.71	0.43	2.84	0.57
AOD	3.67	0.73	4.20	0.67	**0.27**	**0.96**
dlo	4.35	0.18	4.55	0.20	2.72	0.40
GlA	3.81	0.50	3.46	0.50	3.27	0.62
lo	2.47	0.40	2.19	0.60	2.25	0.62
AOV	3.71	0.46	4.05	0.48	1.89	0.77
OB	**4.06**	**0.90**	**0.36**	**0.99**	**0.22**	**0.99**
RG	4.09	0.90	0.37	0.99	0.23	0.99
RV	2.91	0.58	2.82	0.62	2.07	0.66
Total	3.55	0.75	1.47	0.82	0.79	0.89

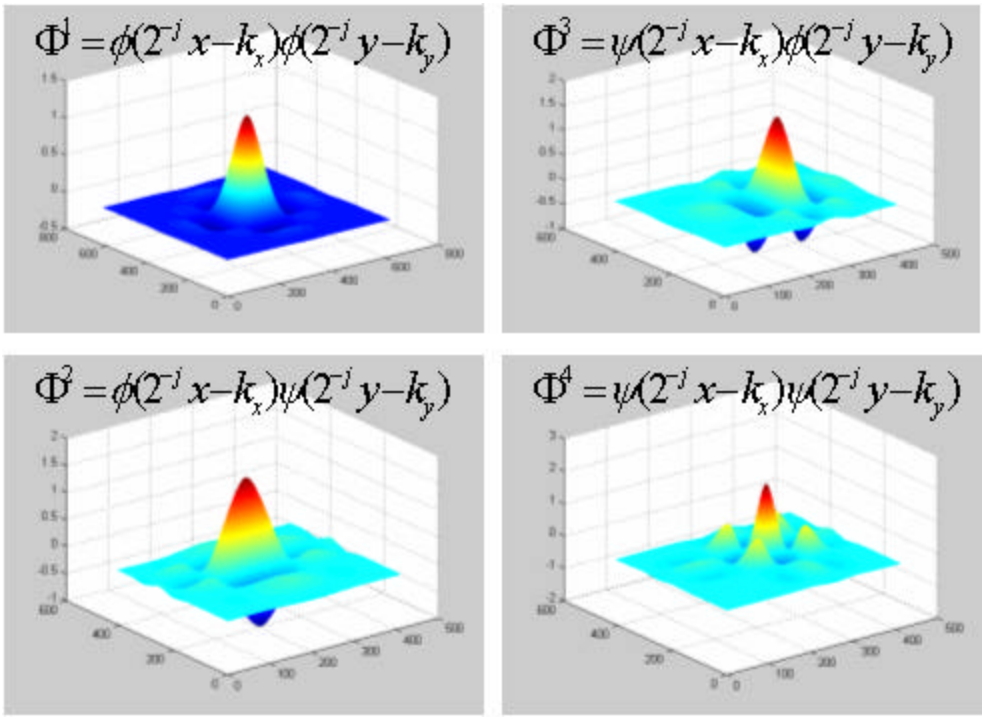

Fig. 1. The four separable 2D wavelet basis functions based on orthogonal *Coiflets* wavelet.

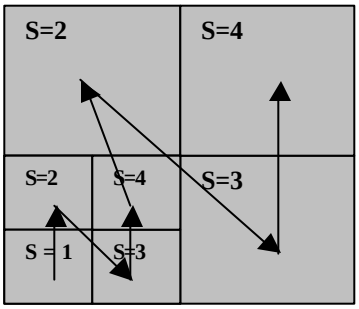

Fig. 2. The progressive order in which registration parameters were estimated.

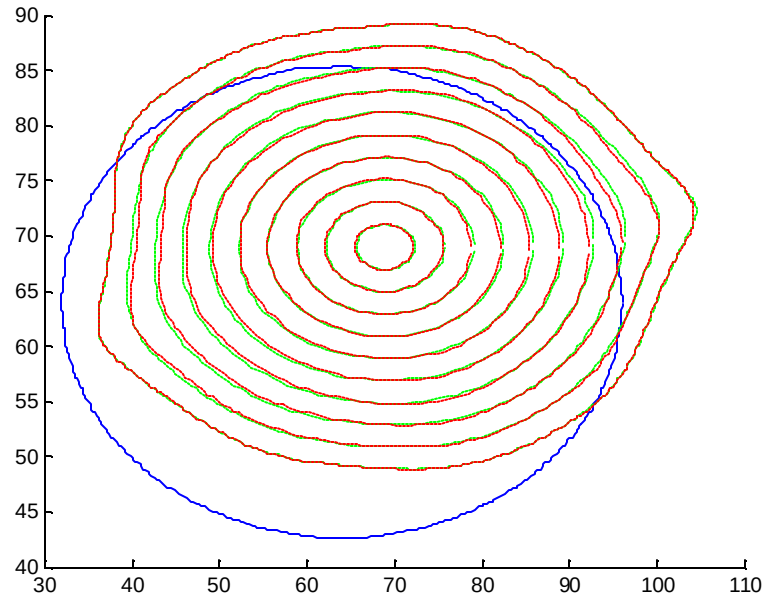

(a)

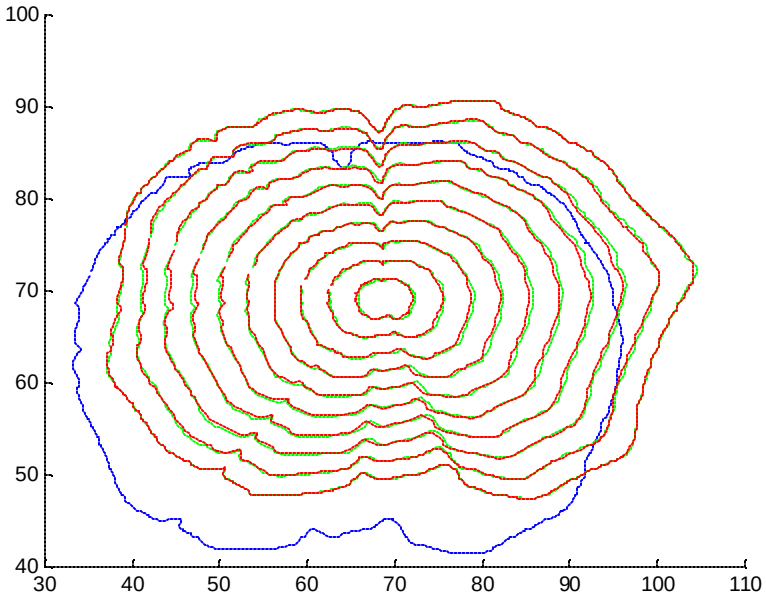

(b)

Fig. 3. The test object: (a) Ellipse and (b) rat brain section (in blue), overlapped by the mapped test object (in red), and the reference object (in dotted green).

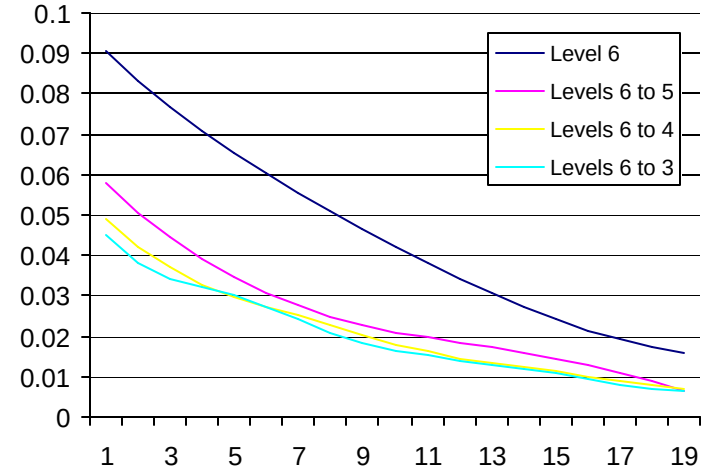

(a)

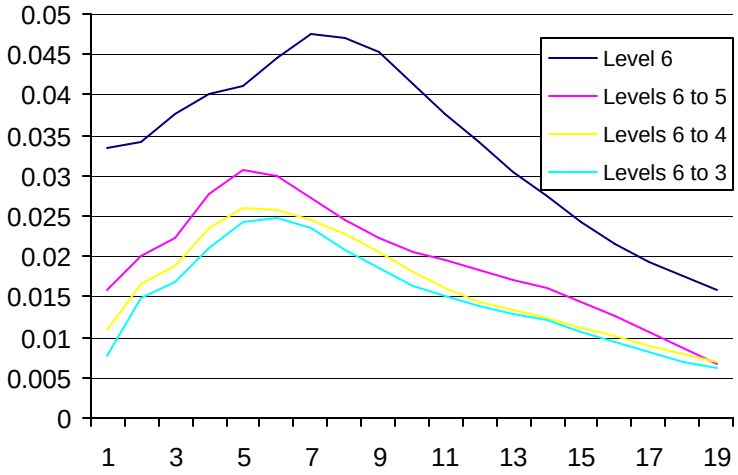

(b)

Fig. 4. (a) Relative actual error, AE/ID, and (b) relative contour error, CE/ID, where an affine transformation was applied to the rat section. The errors are shown for different resolution levels and as a function of concentric layers (external layer (1) through internals layers (2-20)).

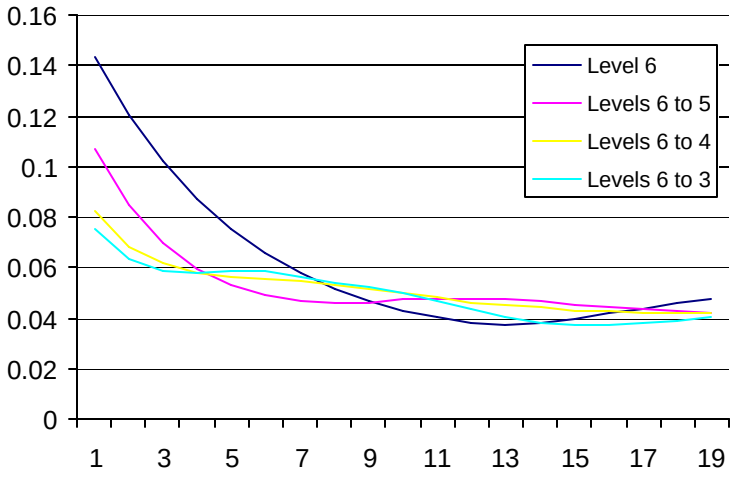

(a)

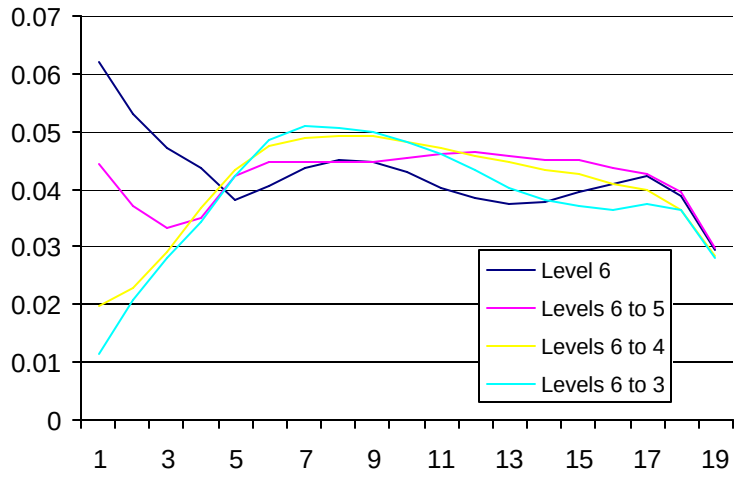

(b)

Fig. 5. (a) Relative actual error, AE/ID, and (b) relative contour error, CE/ID, where an elastic transformation was applied to the rat section. The errors are shown for different resolution levels and as a function of concentric layers (external layer (1) through internals layers (2-20)).

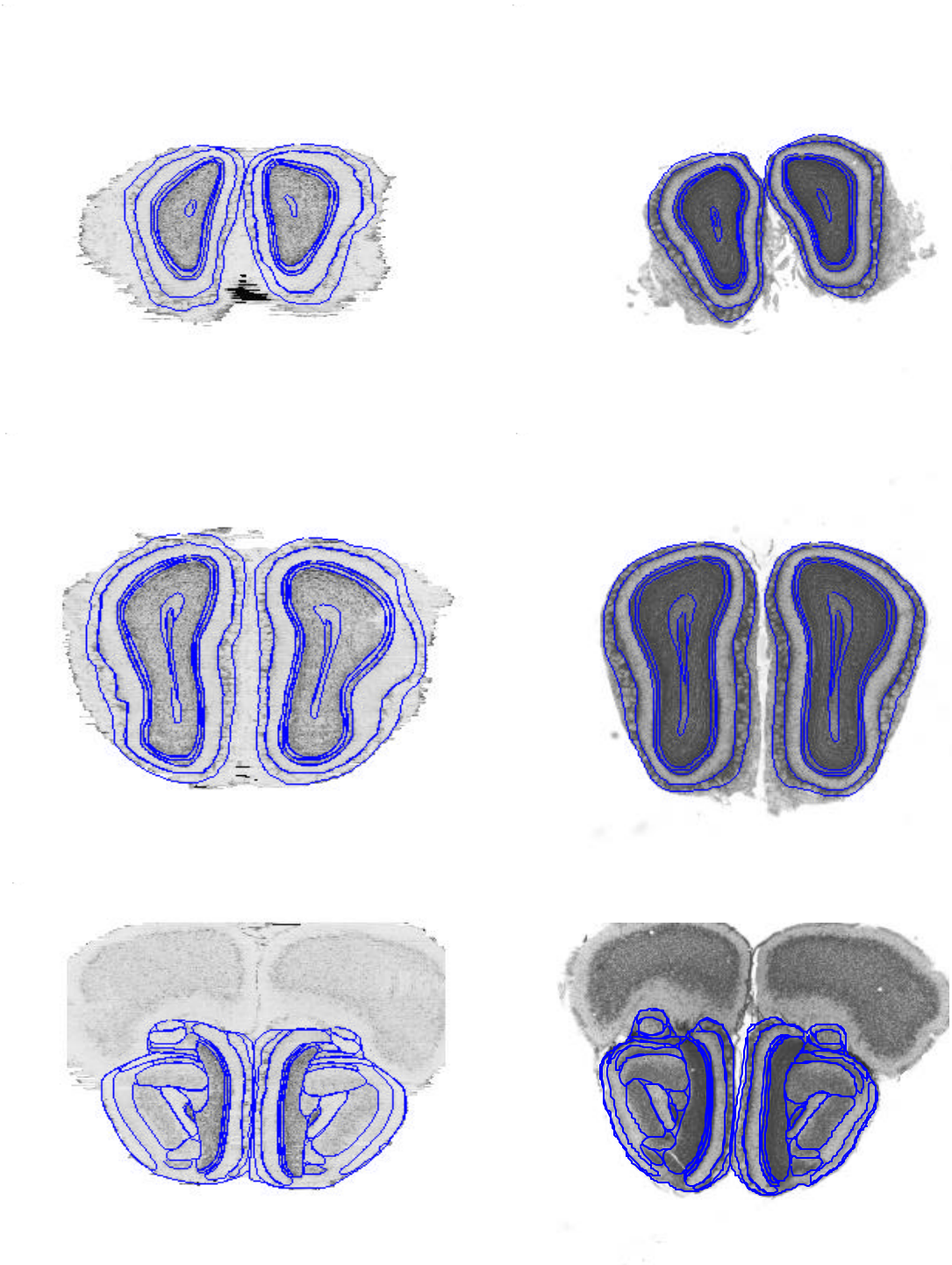

Fig. 6. Matching coronal sections from the atlas (left) and an experimental brain (right). The top pair located at a rostral level, the second pair located at an intermediate level, and the bottom pair located at a caudal level of the olfactory bulbs.

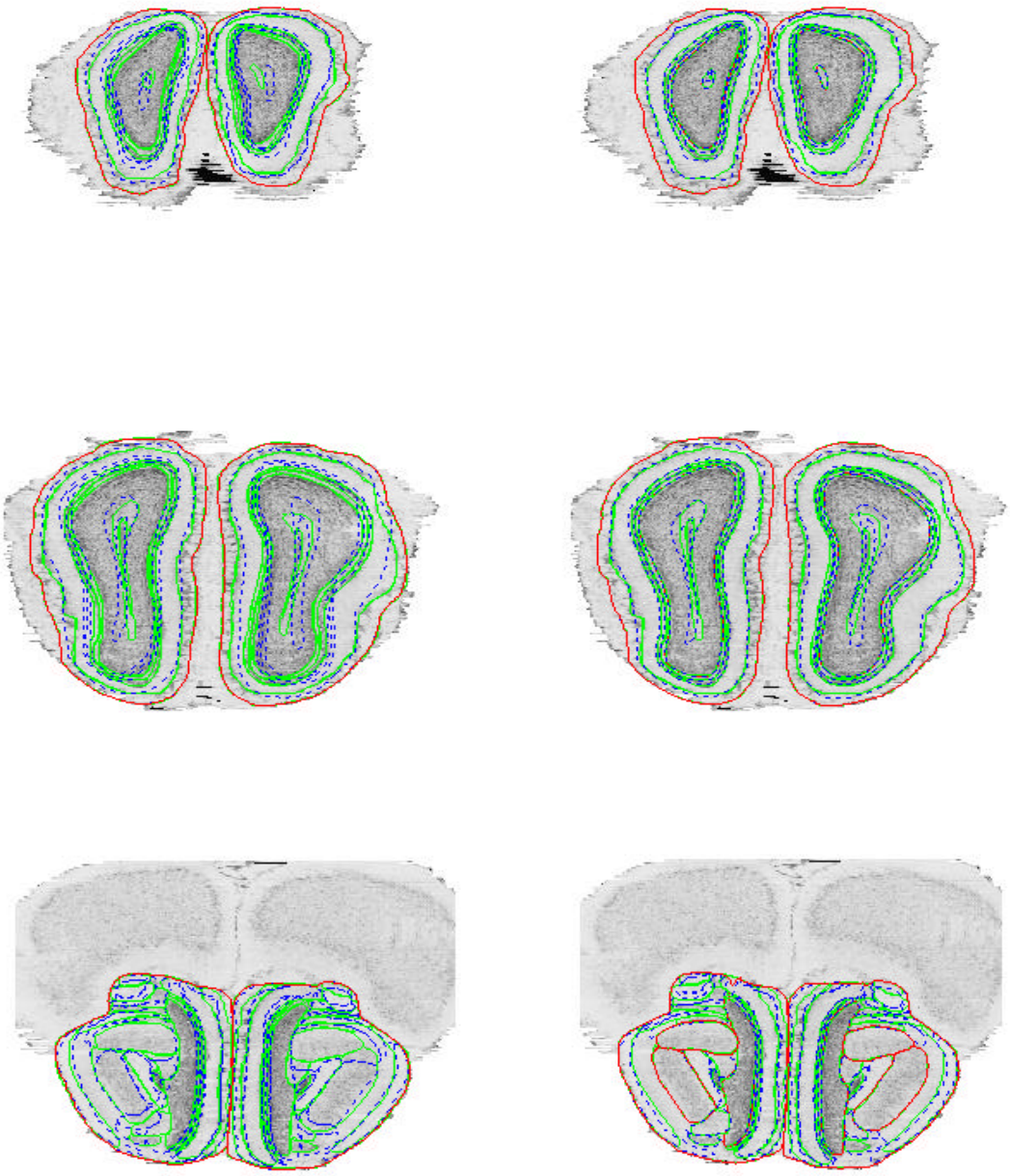

Fig. 7. Reference sections and their structures' contours are shown in dashed/blue lines. On the top of each section are drawn the contours of the corresponding mapped test section where structures used to drive the alignment are shown in red and structures used for validation are shown in green.. Case I (left) and Case II (right) are shown for caudal section (top), intermediate section (middle), and rostral section (bottom).

REFERENCES

[1] I. N. Bankman, *Handbook of Medical Imaging*. San Diego: Academic Press, 2000.

[2] A. W. Toga, *Brain Warping*: Academic Press, 1999.

[3] R. W. Thatcher, M. Hallett, T. Zeffiro, E. R. John, and M. Huerta, *Functional Neuroimaging - Thechnical Foundations*. San Diego: Academic Press, 1994.

[4] L. G. Brown, "A survey of Image Registration Techniques," *ACM Computing Surveys*, vol. 24, pp. 325-376, 1992.

[5] P. A. Van den Elsen, E. J. D. Pol, and M. A. Viergever, "Medical Image Matching- A Review with Classification," *IEEE Engineering in medicine and biology*, pp. 26-39, 1993.

[6] J. West, J. M. Fitzpatric, M. Y. Wang, B. M. Dawant, C. R. Maurer, R. M. Kessler, R. J. Maciunas, C. Barillot, D. Lemoine, A. Collignon, F. Maes, P. Suetens, D. Vandermeulen, P. A. Van Den Elsen, S. Napel, T. S. Sumanaweera, B. Harkness, P. F. Hemler, D. L. G. Hill, D. J. Hawkes, C. Studholme, J. B. Antoine-Maintz, M. A. Viergever, G. Malandain, X. Pennec, M. E. Noz, G. Q. Maguire, M. Pollack, C. A. Pelizzari, R. A. Robb, D. Hanson, and R. P. Woods, "Comparison and Evaluation of Retrospective Intermodality Brain Image Registration Techniques," *Journal of Computer Assisted Tomography*, vol. 21, pp. 554-566, 1997.

[7] H. Lester and S. R. Arridge, "A Survey of Hierarchical Non-linear Medical Image Registration," *Pattern Recognition*, vol. 32, pp. 129-149, 1999.

[8] J. Duchon, "Interpolation des Functions de Deux Variables Suivant le Principle de la Flexion des Plaques Minces," *RAIRO Analyse Numerique*, vol. 10, pp. 5-12, 1976.

[9] J. Meinguet, "Multivariate Interpolation at Arbitrary Points Made Simple," *Z. Angew. Math. Phys.*, vol. 30, pp. 292-304, 1979.

[10] A. Goshtasby, "Registration of Images with Geometric distortions," *IEEE Trans. Geosci. Remote Sensing*, vol. 26, pp. 60-64, 1988.

[11] F. L. Bookstein, "Principal Warps: Thin-Plate Splines and the Decomposition of Deformations," *IEEE Transaction on pattern analysis and machine intelligence*, vol. 11, pp. 567-585, 1989.

[12] M. Gabrani, "Multidimensional Spline Theory and Surface-Based Alignment of Brains," in *ECE*. Philadelphia: Drexel University, 1998.

[13] M. Gabrani and O. J. Tretiak, "Surface-based matching using elastic transformations," *Pattern Recognition*, vol. 32, pp. 87-97, 1999.

[14] R. Bajcsy and S. Kovacic, "Multi-resolution Elastic Matching," *Computer Vision, Graphics and Image Processing*, vol. 46, pp. 1-21, 1989.

[15] C. Broit, "Optimal registration of deformed images," : Univ. Pennsylvania, 1981.

[16] C. Davatzikos, "Nonlinear Registration of Brain Images Using Deformable Models," presented at IEEE Proceedings of MMBIA, 1996.

[17] Y. Amit, "A Nonlinear Variational Problem for Image Matching," *SIAM J. Scientific Comput.*, vol. 15, pp. 207-224, 1994.

[18] T. R. Downie, L. Shepstone, and B. W. Silverman, "A Wavelet Based Approach to Deformable Templates," presented at Image Fusion and Shape Variability Techniques, Leeds, UK, 1996.

[19] J. Deubler and J. C. Olivo, "A Wavelet Based Multiresolution Method to Automatically Register Images," *Journal of Mathematical Imaging and Vision*, vol. 7, pp. 199-209, 1997.

[20] M. Vetterli and J. Kovacevic, *Wavelets and Sub-band Coding*: PrenticeHall, 1995.

[21] G. Strang and T. Nguyen, *Wavelets and Filter Banks*: Wellesley-Cambridge, 1997.

[22] S. Mallat, *A Wavelet Tour of Signal Processing*: Academic Press, 1999.

[23] I. Daubechies, *Ten Lectures on Wavelets*. Philadelphia: Society for Industrial and Applied Mathematics (SIAM), 1997.

[24] S. Gefen, "Wavelet-based Nonlinear Multi-dimensional Registration," in *Electrical and Computer Engineering*. Philadelphia: Drexel University, 2002.

[25] D. Kozinska, O. J. Tretiak, J. Nissanov, and C. Ozturk, "Multidimentional Alignment Using the Euclidean Distance Transform," *Graphical Models and Image Processing*, vol. 59, pp. 373-387, 1997.

[26] C. Ozturk, "Alignment Package for Matlab," : http://cbis.ece.drexel.edu/ICVC/Align/align.html, 1997.

[27] D. W. Marquardt, "An Algorithm for Least-squares Estimation of Nonlinear Parameters," *J. Soc. Indust. Appl. Math.*, vol. 11, pp. 431-441, 1963.

[28] J. Nissanov, J. Eilbert, O. J. Tretiak, S. Gefen, S. Schremmer, C. Gustafson, and L. Bertrand, "3D Atlases - Bridges Between Neurogenomics and Neuroanatomy," presented at IEEE International Symposium on Bio-medical Imaging, Washington DC, 2002.

[29] G. D. Rosen, A. G. Williams, J. A. Capra, M. T. Connolly, B. Cruz, L. Lu, D. C. Airey, K. Kulkarni, and R. W. Williams, "The Mouse Brain Library @ www.mbl.org," presented at Int Mouse Genome Conference, 2000.

[30] C. Gustafson, O. Tretiak, L. Bertrand, and J. Nissanov, "Design and Implementation of Software for Assembly and Browsing of 3D Brain Atlases," *submitted to Computer Methods and Programs in Biomedicine*, 2002.

[31] K. B. J. Franklin and G. Paxinos, *The Mouse Brain in Streotaxic Coordinates*: Academic Press, 1997.